Membrane stretching activates calcium-permeability of a putative channel Pkd2 during fission yeast cytokinesis

Abhishek Poddar[1,#], Yen-Yu Hsu[2,#], Faith Zhang[1], Abeda Shamma[6], Zachary Kreais[6], Clare Muller[1], Mamata Malla[1], Aniruddha Ray[6], Allen Liu[2,3,4,5,*] and Qian Chen[1,*]

[1]: Department of Biological Sciences, The University of Toledo, 2801 West Bancroft Street, Toledo, OH 43606

[2]: Department of Mechanical Engineering, University of Michigan, Ann Arbor, 2350 Hayward Street, Ann Arbor, MI 48109

[3]: Department of Biomedical Engineering, University of Michigan, Ann Arbor, Ann Arbor, MI 48109

[4]: Department of Biophysics, University of Michigan, Ann Arbor, Ann Arbor, MI 48109

[5]: Cellular and Molecular Biology Program, University of Michigan, Ann Arbor, Ann Arbor, MI 48109

[6]: Department of Physics and Astronomy, The University of Toledo, Toledo, OH 43606

#: Equal contributions

*: Co-corresponding authors

Running title: Pkd2 mechanosensitivity

Keywords: Pkd2, calcium, fission yeast, polycystin, cytokinesis, osmotic shock, cytokinetic calcium spike, mechanosensitive channel ,

Abstract

Pkd2 is the fission yeast homolog of polycystins. This putative ion channel localizes to the plasma membrane. It is required for the expansion of cell volume during interphase growth and cytokinesis, the last step of cell division. However, the channel activity of Pkd2 remains untested. Here, we examined the calcium permeability and mechanosensitivity of Pkd2 through in vitro reconstitution and calcium imaging of the *pkd2* mutant cells. Pkd2 was translated and inserted into the lipid bilayer of giant unilamellar vesicles using a cell-free expression system. The reconstituted Pkd2 permeated calcium when the membrane was stretched via hypo-osmotic shock. In vivo, inactivation of Pkd2 through a temperature-sensitive mutation *pkd2-B42* reduced the average intracellular calcium level by 34%. Compared to the *wild type*, the hypomorphic mutation *pkd2-81KD* reduced the amplitude of hypo-osmotic shock-triggered calcium spikes by 59%. During cytokinesis, mutations of *pkd2* reduced by 60% the calcium spikes that accompany the cell separation and the ensuing membrane stretching. We concluded that fission yeast polycystin Pkd2 allows calcium influx when activated by membrane stretching, representing a likely mechanosensitive channel that contributes to the cytokinetic calcium spikes.

Introduction

Polycystins are evolutionarily-conserved calcium-permissive cation channels. Loss of function mutations of human polycystins leads to one of the most common genetic disorders, Autosomal Dominant Polycystic Kidney Disorder (ADPKD) which is diagnosed in 1 in 1000 live births (Hughes et al., 1995; Mochizuki et al., 1996). Homologs of polycystins have been found in most metazoans, including fruit flies and worms (Barr and Sternberg, 1999; Gao et al., 2003), as well as unicellular organisms such as social amoebae (Lima et al., 2014), green algae (Huang et al., 2007) and fission yeast (Palmer et al., 2005).

The fission yeast polycystin homolog Pkd2 is an essential protein required for cell division and growth. Pkd2 localizes to the plasma membrane throughout the cell cycle (Morris et al., 2019). During interphase, it is enriched at cell tips where the putative channel promotes the extension of the cylindrical-shaped fission yeast cells (Sinha et al., 2022). During cytokinesis, Pkd2 moves to the equatorial plane, regulating contractile ring constriction and cell separation (Morris et al., 2019). Without Pkd2, the daughter cells fail to separate. In addition, Pkd2 antagonizes the activity of yeast Hippo signaling pathway SIN (septation initiation network) by modulating its activity and localization during cytokinesis (Sinha et al., 2022). Although fission yeast cytokinesis is accompanied by a temporary increase in intracellular calcium concentration (Poddar et al., 2021), it remains unclear if Pkd2 permeates calcium in this process and how it is activated.

Reconstitution experiments using bottom-up in vitro expression of transmembrane proteins, including ion channels, have become a powerful approach to investigating their functions compared to purified proteins expressed in cells. For expression of certain proteins in cells, growth retardation or lysis of the host cells and low endogenous expression levels attribute

62 to poor production of heterologous recombinant proteins (Laohakunakorn et al., 2020). Despite
63 advances in protein purification, several limitations exist for invitro reconstitution of membrane
64 proteins with complicated structures, such as improper protein function, compromised membrane
65 integrity due to residual detergents, and poor control over the orientation of protein insertion (Jia
66 and Jeon, 2016; Knol et al., 1998; Rigaud and Levy, 2003; Shen et al., 2016; Wingfield, 2015).
67 Cell-free expression (CFE) systems coupling transcription and translation reactions outside the
68 cellular environment have shown the potential to overcome the barriers mentioned above and can
69 be a robust strategy for protein synthesis and investigation (Chong, 2014; Gregorio et al., 2019;
70 Khambhati et al., 2019; Lu, 2017; Rigaud and Levy, 2003). For example, the bacterial
71 mechanosensitive channel MscL is expressed by encapsulating CFE reactions in giant
72 unilamellar vesicles (GUVs) and has been shown to sense physical stimuli (Majumder et al.,
73 2017). Since bacterial lysate lacks membranous components, eukaryotic CFE systems are
74 gaining increasing attention for in vitro production of membrane proteins (Dondapati et al.,
75 2014). Their innate endogenous microsomal structures enable newly synthesized membrane
76 proteins to insert directly into the natural endoplasmic reticulum (ER)-based lipid bilayers
77 without detergents. This eukaryotic CFE-based approach significantly reduces the potential for
78 membrane protein denaturation and favors their proper folding in vitro.
79 In this study, we first expressed the putative channel Pkd2 in a HeLa-based CFE system
80 and reconstituted it in a lipid bilayer. To determine the orientation of Pkd2 in the membrane, we
81 used a pronase digestion assay with *Streptomyces griseus*-derived pronase (Xu et al., 1988). We
82 applied different osmotic pressures to GUVs coexpressing Pkd2 and G-GECO, a fluorescent
83 calcium-sensitive reporter. To determine whether Pkd2 regulates calcium influx in vivo, we
84 employed a GCaMP-based calcium indicator and single-cell imaging to quantify the intracellular

85 calcium level of two *pkd2* mutants. We then induced fast expansion of the plasma membrane
86 using microfluidics-applied osmotic shock and measured the calcium spikes in the *pkd2* mutant
87 cells compared to the *wild type*. Finally, we quantified the constriction and separation calcium
88 spikes, which accompany compression and expansion of the plasma membrane respectively
89 during cytokinesis, in the *pkd2* mutant cells in comparison to the wild type.

90 **Results**

91 **Expressing Pkd2 by using mammalian CFE**

92 We used a CFE system to synthesize this putative channel Pkd2 in vitro. We expressed full-
93 length Pkd2 tagged with superfold GFP (sfGFP) at the C-terminus in a HeLa cell extract-based
94 system. To monitor expression yield, we quantified the fluorescence of Pkd2-sfGFP over 3 hours
95 (**Fig. S1**). The fluorescence increased gradually and reached a plateau after 2 hours. We
96 concluded that Pkd2 is efficiently expressed in our cell-free system.

97 We then determined if the in vitro-synthesized Pkd2 can be reconstituted as a
98 transmembrane protein in supported lipid bilayers with extra reservoir (SUPER) templates (**Fig.**
99 **1A**). The excess lipid bilayer membranes were generated on silica beads by the rupture and
100 fusion of small unilamellar vesicles (SUVs) carrying lipids with negative charges under high
101 ionic strength (Majumder et al., 2018; Pucadyil and Schmid, 2008; Pucadyil and Schmid, 2010).
102 We incubated SUPER templates with the in vitro-translated Pkd2-sfGFP and isolated them by
103 low-speed centrifugation. The supernatant fraction contained most of the CFE reaction, while the
104 pellet fraction included the SUPER templates for different assays (**Fig. 1A**). The expressed
105 protein appeared as a single band of ~108 kDa on an SDS-PAGE gel (**Fig. 1B**), which was
106 consistent with the predicted molecular weight of the fusion protein (MW_{Pkd2} = 78 kDa). The
107 yield was roughly 15 μg from a 10 μl reaction. The lipid-coated beads incubated with pellet

108 fraction became fluorescent after being washed with PBS (**Fig. 1C**), thereby confirming that
109 Pkd2-sfGFP was incorporated into the SUPER templates.

110 Since several Pkd2 homologs, including the human homologs, localize to the ER and
111 plasma membrane (Gonzalez-Perrett et al., 2001; Hughes et al., 1995; Protchenko et al., 2006),
112 we investigated whether Pkd2 similarly translocate into endogenous microsomal structures. We
113 applied a high-speed airfuge assay to CFE-expressed Pkd2, labeled with fluorescently tagged
114 lysine, Green lysine, to isolate supernatant and pellet fractions; the latter presumably contained
115 microsomes (**Fig. S2A**). The majority of Pkd2 was in the pellet, while the amount of Pkd2 in the
116 supernatant decreased as the washing cycles was increased (**Fig. S2B**). This indicated that ER
117 fragments might recognize translocons and membrane protein chaperones to promote Pkd2
118 insertion into microsomes. When the pellet or supernatant fractions were added to the SUPER
119 templates, only the beads incubated with the pellet fraction were fluorescent (**Fig. S2C**). We
120 concluded that in vitro-expressed Pkd2 translocates into microsomal fragments, which
121 subsequently fused with the SUPER templates.

122 **Reconstituted Pkd2 responds to osmotic pressure to permeate calcium**

123 We next determined the orientation of Pkd2 in the lipid bilayer membranes on SUPER templates
124 using an image-based pronase protection assay. Alpha-fold (Jumper et al., 2021) and other
125 transmembrane helices projection software predicted that Pkd2 possesses an N-terminal
126 extracellular domain and a putative C-terminal cytoplasmic tail (**Fig. S3A**). Depending on the
127 orientation of Pkd2-sfGFP in the lipid bilayer, sfGFP will either be exposed to pronase or be
128 protected from degradation (**Fig. S3B**). Based on our previous work on reconstituting nuclear
129 envelope proteins SUN1 and SUN2 in SUPER templates (Majumder et al., 2018), we predicted
130 that Pkd2 would insert into the excess lipid bilayer membranes with its C-terminus orienting

131 outwards. We observed that the fluorescence of in vitro-translated Pkd2-sfGFP disappeared
132 following pronase treatment (**Fig. S3C**). We concluded that Pkd2 is inserted in microsomal
133 fragments in an orientation that positions its C-terminus on the cytosolic side. For the GUVs we
134 used in our experiment, the C-terminus of Pkd2-sfGFP would be in the lumen of the vesicle, an
135 orientation consistent with their predicted topology in cells (**Fig. 2A**) since CFE reactions were
136 encapsulated in vesicles.

137 We next determined whether reconstituted Pkd2 alone is calcium permissive. We
138 encapsulated CFE-expressed Pkd2 in GUVs generated using continuous droplet interface
139 crossing encapsulation (cDICE) (Bashirzadeh et al., 2021; Van de Cauter et al., 2021) and
140 monitored calcium entry in GUVs (**Fig. 2B**). A genetically-encoded calcium fluorescent reporter,
141 G-GECO, was used to detect calcium entry into vesicles (Majumder et al., 2017). There was no
142 G-GECO fluorescence in GUVs under iso-osmotic conditions with or without Pkd2 expression
143 (**Fig. 2C**), indicating that CFE-expressed Pkd2 is mostly non-permeable to calcium without a
144 stimulus.

145 To determine whether Pkd2 can become calcium-permeable upon mechanical stimulus,
146 we stretched the membrane of Pkd2-expressing GUVs with hypo-osmotic shock. We added
147 water to the external solution of the GUVs. The G-GECO fluorescence in Pkd2-embedded GUVs
148 gradually increased under a hypo-osmotic condition of 100 mOsm, compared to those without
149 Pkd2 (**Fig. 2C**). The fluorescence increase was proportional to calcium concentrations in the
150 external solution (**Fig. S4**). When gadolinium chloride ($GdCl_3$), a non-specific stretch-activated
151 ion channel blocker, was added to the external solution, it blocked the fluorescence increase of
152 G-GECO inside those Pkd2-expressing GUVs under same conditions (**Fig. 2D**). As expected,
153 the peak fluorescence intensities of GUVs increased proportionally to the strength (40-100

154 mOsm) and duration (0-20 mins) of hypo-osmotic shock (**Fig. 2E and F**). We concluded that
155 Pkd2 is calcium-permeable under the mechanical stimulus of membrane stretching.

156 **Intracellular calcium level was lower in *pkd2* mutants**

157 To determine if calcium-permissive Pkd2 regulates calcium homeostasis in fission yeast cells,
158 we measured the calcium level of *pkd2-81KD,* a hypomorphic mutant with growth and
159 cytokinesis defects even at the permissive temperature (Morris et al., 2019). We employed the
160 ratiometric indicator GCaMP-mCherry to measure the intracellular calcium level of single cells
161 (Poddar et al., 2021) by quantifying the ratio of fluorescence intensity of GCaMP to that of
162 mCherry (**Fig. 3A**). At 25°C, the intracellular calcium level of mutant cells (n > 450) decreased
163 only slightly (3%) compared to *wild type* cells (**Fig. 3B**). Next, we measured the calcium level of
164 a novel temperature-sensitive *pkd2* mutant at the restrictive temperature (Sinha et al., 2022). At
165 36°C, the average calcium level of *pkd2-B42* cells was 34% lower than *wild type* cells (**Fig. 3C**
166 **and D**). To rule out the possibility that reduced calcium concentration was an indirect result of
167 either cytokinesis or growth defects of the *pkd2* mutant, we examined two other temperature-
168 sensitive mutants, *sid2-250* and *orb6-25*. The former fails in cytokinesis, and the latter is
169 defective in cell growth (Balasubramanian et al., 1998; Verde et al., 1998). In comparison to
170 *pkd2-B42*, the intracellular calcium concentration of the *sid2-250* mutant cells were only slightly
171 lower (by 13%) than *wild type* cells at 36°C (**Fig. S5A and B**). This was despite their much
172 stronger cytokinesis defect compared to *pkd2-B42*, evident in the substantially increased cell
173 length (**Fig. S5A**). Contrary to *pkd2-B42*, *orb6-25* almost doubled the intracellular calcium level
174 with a far higher frequency of cells exhibiting elevated calcium concentrations **(Fig. S5B)**. We
175 concluded that putative channel Pkd2 contributes significantly to the maintenance of intracellular
176 calcium levels.

177 Lastly, we determined whether over-expression of Pkd2 interfered with intracellular
178 calcium regulation. We over-expressed Pkd2 by replacing its endogenous promoter with a strong
179 inducible promoter, 3nmt1 (Maundrell, 1990). Under the inducing condition, intracellular
180 calcium levels of mutant cells were similar to that of *wild type* cells (**Fig. S5C-D**). We concluded
181 that over-expression of Pkd2 alone is not sufficient to alter intracellular calcium levels.

182 **Osmotic shock-induced calcium spikes were reduced in *pkd2* mutants**

183 We examined whether Pkd2 promotes calcium spikes triggered by plasma membrane stretching
184 in vivo. In yeast, an abrupt drop in extracellular osmolarity triggers a sharp increase in
185 intracellular calcium levels (Batiza et al., 1996). Such calcium spikes, accompanied by cell
186 volume expansion, raise the intracellular calcium level by up to five-fold (Poddar et al., 2021).
187 These spikes can be captured at the single-cell level in a microfluidic device.

188 We first determined whether such calcium spikes depend on influx from the media, a
189 process that plasma membrane localized Pkd2 likely regulates. We first trapped the *wild type*
190 cells in a microfluidic imaging chamber infused with the isosmotic EMM media (**Fig. 4A**). After
191 switching to EMM plus 1.2M sorbitol for 30 minutes, we dropped the extracellular osmolarity by
192 more than 1,300 mOsm by switching back to EMM (**Fig. 4A, S6A**). This shock caused the
193 average width of *wild type* cells to increase significantly (**Fig. 4B**). As expected, this was
194 accompanied by calcium spikes (**Fig. 4C**). In comparison, removing calcium from EMM media
195 during hypo-osmotic shock reduced average amplitude of calcium spikes by 40% (**Fig. S6C, E,**
196 **and F**). Similarly, 2mM EGTA in EMM media resulted in a 52% decrease in the amplitude of
197 calcium spikes (**Fig. S6D-F).** We concluded that extracellular calcium contributes significantly
198 to calcium spikes induced by hypo-osmotic shock.

199 We then determined whether Pkd2 contributes to osmotic shock-induced calcium spikes.
200 We measured the spikes in *pkd2-81KD* mutant cells stimulated with hypo-osmotic shock. Like
201 *wild type* cells, *pkd2-81KD* mutant cells expanded their width after shock, but comparably less
202 (**Fig. 4B**). Peak amplitude of the spikes in *pkd2-81KD* cells was 59% lower than in *wild type*
203 cells (**Fig. 4C and D**). The amplitude of the spikes in *pkd2-B42* cells was similarly reduced by
204 62% **(Fig. 4D).** On average, the calcium level in *pkd2-81KD* returned to baseline sooner than in
205 *wild type* after shock **(Fig. 4E)**. We concluded that Pkd2 contributes significantly to calcium
206 influx triggered by hypo-osmotic shock in vivo.

207 **Pkd2 mutations reduced the separation calcium spikes during cytokinesis**

208 Besides the stress induced calcium transients, two separate calcium spikes accompany the fission
209 yeast cytokinesis (Poddar et al., 2021)**.** The constriction spikes are concurrent with the cleavage
210 furrow ingression and the membrane compression whose force is provided by the actomyosin
211 contractile ring **(Fig. 5A)**. The other, termed separation spike is accompanied by the cell
212 separation, a process concurrent with the membrane stretching **(Fig. 5A)**.

213 First, we compared the constriction spikes in the *pkd2* mutant cells to those in the wild
214 type cells. We carried out the time-lapse calcium imaging in the cells expressing the actomyosin
215 contractile ring marker Rlc1-Tdtomato together with GCaMP throughout the ring assembly and
216 constriction **(Fig. 5B).** As we shown before (Poddar et al., 2021), the GCaMP fluorescence of the
217 *wild type* cells increased by an average of 2-fold within 4 minutes after the start of the ring
218 constriction. In comparison, such fluorescence increased by more than 4-fold in either *pkd2-*
219 *81KD* or *pkd2-B42* cells following the ring constriction **(Fig. 5C).** Next, we extracted individual
220 calcium spikes using computer-assisted image analysis and quantified their amplitudes (see
221 Methods and Materials). The average amplitude of constriction spikes in the *pkd2* mutant cells

222 increased more than 2.5-folds, compared to those of the wild type cells **(Fig. 5D).** We conclude
223 that Pkd2 is not essential for the constriction spikes during cytokinesis.

224 Next, we applied similar methods to compare the separation spikes of the *pkd2* mutant
225 cells to those of the wild type. We tracked the last step of cytokinesis, when two daughter
226 physical separate and their new ends emerge, through bright-field microscopy coupled with the
227 calcium imaging **(Fig. 5E).** Consistent with our previous observation (Poddar et al., 2021), the
228 GCaMP fluorescence of the wild type cells increased ~1.8-fold within 2 minutes of cell
229 separation in either both or one daughter cell. In comparison, such fluorescence increased was
230 more than 50% smaller in either *pkd2-81KD* or *pkd2-B42* cells **(Fig. 5F).** Next, we extracted
231 individual calcium spikes in these separating cells using computer-assisted image analysis and
232 quantified their amplitudes (see Materials and Methods). As expected, the average amplitude of
233 the spikes identified in *pkd2-81KD* and *pkd2-B42* mutant cells decreased by 45% and 60%
234 respectively **(Fig. 5G).** We conclude that Pkd2 contributes to the separation calcium spikes at the
235 end of cytokinesis.

236 **Discussion**

237 In this study, we determined the calcium permeability and activation mechanism of putative
238 fission yeast channel Pkd2. In vitro reconstitution established Pkd2 as calcium-permeable under
239 membrane tension. Calcium imaging of *pkd2* mutant cells demonstrated this essential protein's
240 critical role in regulating calcium homeostasis and adaptation to hypo-osmotic shock.

241 In vitro-reconstituted Pkd2 in GUVs allowed the passage of calcium ions in a force-
242 dependent manner. Mechanical activation of Pkd2 was proportional to the extent of membrane
243 stretching, suggesting that only a small fraction of the transmembrane protein was activated at
244 the lower end of the applied force. Compared to calcium spikes in the yeast cells, the calcium

245 influx mediated by Pkd2 in vitro was relatively slow. This is likely due to the small amount of
246 reconstituted Pkd2 in the membrane. Another reason may be that our GUVs do not have calcium
247 buffer capabilities other than G-GECO. Nevertheless, our minimal system demonstrated that
248 Pkd2 is calcium-permeable in response to membrane stretching.

249 The calcium permeability of reconstituted Pkd2 is consistent with the significantly
250 reduced intracellular level of *pkd2* mutant cells. Our in vivo data has provided the first line of
251 evidence that Pkd2 mediates calcium homeostasis in fission yeast cells. It remains to be
252 determined whether Pkd2 is also permeable to other cations such as potassium similar to human
253 polycystins (Liu et al., 2018).

254 The calcium spikes triggered by hypo-osmotic shock likely come from calcium influx
255 and internal release. Removal of extracellular calcium did not quench calcium spike completely,
256 suggesting the calcium release from the internal sources must contribute to the calcium spikes.
257 These could come from either ER or vacuoles, the main intracellular calcium storage of yeast
258 cells (Pittman, 2011).

259 Consistent with the mechanosensitivity of Pkd2 in vitro, it also plays a critical role in
260 adaptation to hypo-osmotic shock when tension of the plasma membrane increases. Our result
261 confirms the long-standing hypothesis that stretch-activated yeast channels likely contribute to
262 osmotic adaptation whose identities have nevertheless remained unknown (Batiza et al., 1996).
263 Considering its localization on the plasma membrane and its force-sensitivity, Pkd2 likely allows
264 the direct influx of calcium that contributes to adaptation after hypo-osmotic shock (Nakayama
265 et al., 2012). However, it is worth noting that mutations of *pkd2* reduced calcium spike even
266 more than removal of external calcium following hypo-osmotic shock. This strongly suggests

267 that Pkd2 not only regulates calcium influx, but also internal release of calcium during the
268 spiking events.

269 The function of Pkd2 in regulating osmotic adaptation bears some similarities to that of
270 mechanosensitive MscC channels, but there are some critical differences. Msy1 and Msy2 are
271 fission yeast homologs of the small bacterial conductance mechanosensitive channel MscS
272 (Nakayama et al., 2012). Like Pkd2, Msy1 and Msy2 play a crucial role in adaptation to hypo-
273 osmotic shock. However, unlike Pkd2, they localize to the endoplasmic reticulum (ER)
274 (Nakayama et al., 2012). More surprisingly, deletion of both fission yeast MscS channels leads to
275 enhanced calcium spikes following hypo-osmotic shock (Nakayama et al., 2012), contrary to the
276 phenotype of *pkd2-81KD* mutant cells. The potential interlink between polycystin and MscS
277 channels will require further analysis.

278 The force-sensitive nature of putative channel Pkd2, combined with its localization on the
279 plasma membrane, makes it an ideal candidate to sense membrane tension and regulate turgor
280 pressure homeostasis during cell growth. The key phenotype of *pkd2* mutants is their failure to
281 maintain turgor pressure required for both tip extension and cell separation. This putative
282 channel could play a critical role in maintaining turgor pressure during cell growth, as the cell
283 volume expands. Pkd2 is a potential candidate for the known mechanosensitive channel
284 regulating the turgor pressure of fission yeast (Zhou and Kung, 1992).

285 The reduced separation calcium spikes in the *pkd2* mutant cells strongly suggests that the
286 putative Pkd2 channel may contribute directly to the calcium influx during the cell separation.
287 Pkd2 is likely activated by the membrane stretching as a result of the daughter cells increasing
288 their volume and forming the new ends. In contrary to the separation spikes, the constriction
289 spikes increased in the *pkd2* mutant cells, suggesting that other channels may contribute to this

290 calcium spike. The increased constriction spike, nevertheless, is consistent with the accelerated
291 ring constriction observed in the *pkd2* mutant cells (Morris et al., 2019).
292 The calcium permeability of Pkd2 is similar to that of mammalian polycystins, but its
293 mechanosensitivity is distinct. Like Pkd2, human polycystin channels also regulate intracellular
294 calcium levels (Liu et al., 2018; Wang et al., 2019). Moreover, of the two mammalian
295 homologues, polycystin-1 is sensitive to mechanical stimulus (Forman et al., 2005). However,
296 the mammalian polycystin channels mostly localize to primary cilia where they are activated by
297 mechanical force from fluid flow (Nauli et al., 2003).
298 Our results support the hypothesis that Pkd2 is a calcium-permissible ion channel
299 activated by membrane stretching during osmotic adaption and cytokinesis.
300
301

302 **Materials and Methods**

303 **DNA construct**

304 Pkd2-sfGFP was constructed through High-Fi DNA Assembly (NEB). All PCR reactions were
305 carried out with Q5 High-Fidelity DNA Polymerase (NEB #M0491). The cDNA of Pkd2 was
306 amplified from the plasmid Pkd2-EGFP-N1 (Lab stock) using the forward primer
307 AACCCTCAAAAGACAAGACCATGAGGCTTTGGAGAAGCCC and the reverse primer,
308 AAGAATTCGTCGACCTCGAGACGAAAAGCATTGTTAGGTA. The vector pAV0714
309 (Vjestica et al., 2020) was amplified using the forward primer,
310 TACCTAACAATGCTTTTCGTCTCGAGGTCGACGAATTCTT and the reverse primer,
311 GGGCTTCTCCAAAGCCTCATGGTCTTGTCTTTTGAGGGTT. The PCR products were then
312 digested with DpnI for 1 hour at 37ºC and purified with Macherey-Nagel NucleoSpin Gel and
313 PCR Clean-up kit (NC0389463). The purified fragments were assembled through HiFi DNA
314 Assembly (NEB, E2621S) to generate the Pkd2-sfGFP construct (QC-V199).

315 To generate Pkd2-His_6 and Pkd2-sfGFP-His_6 for the HeLa CFE reaction, the $SUN1^{FL}$-
316 His_6 construct in pT7-CFE1-Chis (Majumder et al., 2018) was used as a template for Gibson
317 assembly cloning. Initially, Pkd2 was amplified from QC-V199 using the primers Pkd2 –
318 Forward: CCACCACCCATATGGGATCCGAATTCATGAGGCTTTGGAGAAGCCC and
319 Pkd2 – Reverse:
320 CTCGAGTGCGGCCGCGTCGACTTAACGAAAAGCATTGTTAGGTAATGG with Phusion
321 High-Fidelity DNA Polymerase. The DNA of Pkd2–sfGFP was amplified from QC-V199 using
322 the primers Pkd2 – sfGFP – Forward:
323 CACCCATATGGGATCCGAATTCATGAGGCTTTGGAGAAGCCCAC and Pkd2 – sfGFP –
324 Reverse: CGAGTGCGGCCGCGTCGACCTTATAAAGCTCGTCCATTCCGTGAG. The next
325 step was to insert Pkd2 or Pkd2-sfGFP into pT7-CFE1-CHis downstream from the T7 promoter

326 construct by replacing $SUN1^{FL}$ with Pkd2 in the pT7-CFE1-CHis construct (Thermo Fisher
327 Scientific). To remove $SUN1^{FL}$ from the pT7-CFE1-$SUN1^{FL}$-His_6 construct (Majumder et al.,
328 2019) as the backbone, we used primers pT7-CFE-Forward:
329 GAATGGACGAGCTTTATAAGGTCGACGCGGCCGCACTC and pT7-CFE-Reverse:
330 GCTTCTCCAAAGCCTCATGAATTCGGATCCCATATGGGTGGTG with Phusion High-
331 Fidelity DNA Polymerase for PCR amplification. Afterward, the resulting PCR products, Pkd2,
332 Pkd2-sfGFP, and pT7CFE-CHis, were digested with DpnI for 1 hour at 37°C and subsequently
333 purified with the QIAquick Gel Extraction Kit (Qiagen #28704). They were ligated with
334 homemade Gibson Master Mix (**Table S1**) to create pT7-CFE1-Pkd2-CHis and pT7-CFE1-
335 Pkd2-sfGFP-CHis constructs.

336 **CFE reaction**

337 We used the 1-Step Human Coupled IVT Kit (Thermo Fisher Scientific #88881) to produce
338 Pkd2 protein in vitro. The reaction was carried out based on the manufacturer's protocol. Briefly,
339 1 µl plasmid DNA (~500 ng/µl) was used for one 10 µl reaction. G-GECO plasmid was used in a
340 previous study (Majumder et al., 2017). CFE reactions were carried out at 30°C for 3 hours.
341 Pkd2-sfGFP expression was measured on a fluorescence plate reader (Biotek Synergy H1).

342 **SUPER template generation**

343 Supported bilayer with excess membrane reservoir (SUPER) templated beads were generated
344 following a published protocol (Neumann et al., 2013). For SUPER template formation, 25 µl of
345 small unilamellar vesicle (SUV) solution was fused with 2 µl of 5 µm silica beads (Bangs
346 Laboratories) in the presence of 1 M NaCl. The final SUPER templated beads were washed with
347 PBS twice by centrifuging at 200 *g* for 2 minutes and then resuspended in 30 µl of milli-Q water
348 at a final concentration of ~9.6×10^6 beads/ml. The SUPER template stock can be stored at room
349 temperature for 3 hours.

350 For SUV generation, 75% 1,2-dioleoyl-*sn*-glycero-3-phosphatidylcholine (DOPC),
351 24.9% cholesterol, and 0.1% Rhod-PE for a final concentration of 1 mM were mixed and dried
352 under vacuum for 1 hour. 1 ml milli-Q water was then added, and the tube was thoroughly
353 vortexed. The mixture was then passed through a liposome-extruder (T&T Scientific, Knoxville,
354 TN) with 100 nm porous membrane for 11 times to generate SUVs.

355 **Vesicle encapsulation system**

356 Vesicles were generated by modifying the continuous droplet interface crossing encapsulation
357 (cDICE) method. The device contains a rotor chamber made with clear resin using a 3D printer
358 (Formlabs) mounted on the servo motor of a benchtop stir plate. The procedure involves an inner
359 solution (IS), outer solution (OS), and lipid-in-oil solution (LOS). HeLa-based CFE reactions
360 with the addition of 5% OptiPrep (to increase the density to aid sedimentation of GUVs) were
361 prepared as the IS. OS stock (115 mM HEPES, 23 mM $MgCl_2$, 1.15M KCl, 770 mM glucose)
362 was diluted with Milli-Q water to the same osmolarity matching that of the IS. The LOS consists
363 of 40% DOPC, 30% DOPE, 29.9% cholesterol, and 0.1% Rhod-PE in mole percentage with a
364 total lipid concentration of 0.4 mM was thoroughly mixed with the desired volume of 1:4
365 mineral oil:silicon oil by vortexing for at least 10 seconds. The water-in-oil emulsion was first
366 generated by vigorously pipetting CFE reactions in 500 µL of LOS ~10 times. 700 µL of
367 aqueous OS, 5 mL of LOS and the water-in-oil emulsion were then sequentially added into the
368 cDICE chamber rotating at 700 rpm. After 2 minutes of rotation, vesicles accumulating in the OS
369 near the chamber wall could be gently collected from the capped hole near the outer edge of the
370 chamber.

371 **Airfuge fractionation assay**

372 After the CFE reaction was completed, it was collected in a 1.5 mL microcentrifuge tube and

373 then mixed well with 30 µl of extraction buffer (20 mM HEPES-KOH, pH 7.5, 45 mM
374 potassium acetate, 45 mM KCl, 1.8 mM magnesium acetate, 1 mM dithiothreitol (DTT)). 40 µl
375 of the mixture was then transferred to an ultracentrifuge tube and centrifuged at around 100,000
376 *g* for 15 minutes at room temperature using an airfuge (Beckman Coulter). After the
377 centrifugation, 20 µl of the supernatant was carefully recovered and transferred to a 1.5 mL
378 microcentrifuge tube without disturbing the pellet, and the remaining 20 µl of pellet fraction was
379 resuspended by pipetting up and down to thoroughly mix before transferring to another
380 microcentrifuge tube. The centrifugation cycles mentioned above can be repeated multiple times,
381 as shown in **Fig. S2A**. To investigate the protein incorporation, 2 µl of SUPER templated beads
382 were added and incubated with the supernatant and pellet fractions respectively for 30 minutes at
383 room temperature and then centrifuged at 300 *g* for 3 minutes. After the centrifugation, SUPER
384 templated beads were visible as a small white pellet, and the remaining supernatant was collected
385 as the final pellet fraction. The SUPER template pellets were washed twice with PBS by
386 centrifuging at 200 *g* for 2 minutes and then resuspended in 30 µl of milli-Q water at a final
387 concentration of ~9.6×10^6 beads/ml. Following the recovery of fractions, the amount of cell-free
388 expressed Pkd2 in each fraction can be determined by visualizing fluorescence proteins on an
389 SDS-PAGE gel.

390 **Pronase digestion assay**

391 Lyophilized *S. griseus* pronase (Roche) was dissolved in Milli-Q water to a stock concentration
392 of 6 mg/ml and stored at 4°C for a maximum of 3 days. After 1 hour of incubation of CFE
393 reactions with SUPER templates, the beads were pelleted by centrifugation at 300 *g* for 3
394 minutes. The supernatant was then gently removed and collected for fluorescence gel imaging.
395 The remaining bead pellets were washed twice with 1 ml of PBS (Ca^{2+} and Mg^{2+}-free, pH 7.5)

396 by centrifugation at 200 *g* for 2 minutes, followed by resuspension in 20 μl of PBS. Next, 10 μl
397 of the SUPER templated beads in PBS was incubated with 5 μl of pronase stock solution (6
398 mg/ml) at room temperature for 15 minutes. The final concentration of pronase was 2 mg/ml,
399 and the other 10 μl of beads were used for observing the protein incorporation as a control.
400 Confocal fluorescence images were taken 15 minutes after the addition of pronase.

401 **Confocal fluorescence microscopy and in-gel imaging of in vitro reconstituted Pkd2.**

402 All images were acquired using an oil immersion 60×/1.4 NA Plan-Apochromat objective with
403 an Olympus IX-81 inverted fluorescence microscope (Olympus, Japan) controlled by
404 MetaMorph software (Molecular Devices, USA) equipped with a CSU-X1 spinning disk
405 confocal head (Yokogawa, Japan), AOTF-controlled solid-state lasers (Andor, Ireland), and an
406 iXON3 EMCCD camera (Andor). Images of sfGFP and lipid fluorescence were acquired with
407 488 nm laser excitation at an exposure time of 500 ms and with 561 nm laser excitation at an
408 exposure time of 100 ms, respectively. Each acquired image contained ~5 lipid bilayer vesicles
409 or ~10 lipid-coated beads that had settled upon a 96-well glass-bottom plate or a coverslip,
410 respectively. Three images were taken at different locations across a well or coverslip for an
411 individual experiment. Three independent repeats were carried out for each experimental
412 condition. Samples were always freshly prepared before each experiment.

413 FluoroTect Green lysine-tRNA (green lysine) was purchased from Promega. In-gel
414 imaging of Pkd2-sfGFP or Pkd2 was carried out on a Sapphire biomolecular imager (Azure
415 Biosystems). Samples were not heated to retain in-gel sfGFP and green lysine fluorescence.

416 **Image analysis**

417 To quantify the fluorescence inside the lipid bilayer vesicles, all images were analyzed using
418 MATLAB. All data are included for analysis without blinding. Since all the vesicles were

419 labeled with rhodamine PE, the edges/boundaries of vesicles were first detected and isolated,
420 corresponding to the red fluorescence rings using the function 'imfindcircles' embedded in
421 MATLAB. Averaged background intensity measurements were then performed for each image
422 by the average fluorescence (of all pixels), excluding the area of vesicles defined by the code in
423 MATLAB from the previous step. For quantification, the final fluorescence intensity of each
424 vesicle was obtained by averaging the fluorescence of all the pixels inside the vesicles after
425 subtracting the average background intensity. For the box plots marking the first and third
426 quartile and the median in **Fig. 2F**, each data point represents the fluorescence of one vesicle
427 after normalization with respect to the average background subtracted fluorescence intensity of
428 vesicles corresponding to the cell-free expressed proteins at time zero under each condition.
429 Since there are two independent variables, time and osmotic condition/osmolarity, statistical
430 analysis was performed using two-way ANOVA followed by Dunnett's post-hoc test for all data
431 among all groups throughout the whole experiment. The quantitative data was
432 compared/analyzed between the individual groups at a certain time followed by a two-tailed *t*-
433 test with a significance level of 0.05. $P < 0.05$ was considered statistically significant. P values
434 are indicated as *: $P < 0.05$; **: $P < 0.01$; ***: $P < 0.001$.

435 **Yeast genetics and cell culture**

436 We followed the standard protocols for yeast cell culture and genetics (Moreno et al., 1991).
437 Tetrads were dissected with a Spore+ micromanipulator (Singer, UK). All the fission yeast
438 strains used in this study are listed in **Supplemental Table S2**.

439 **Microscopy of fission yeast cells**

440 For microscopy, cells were first inoculated in a YE5S medium for two days at 25°C. 1 ml of the
441 exponentially growing cell culture, at a density between 5×10^6/ml and 1.0×10^7/ml, was harvested

442 by centrifugation at 4,000 rpm for 1 min. They were washed three times with synthetic EMM
443 medium ([Ca^{2+}] = 107 μM) and re-suspended in 1 ml of EMM before proceeding for
444 microscopy. 20 μl of the resuspended cells were spotted in a 10-mm Petri dish with a glass
445 coverslip (#1.5) at the bottom (D35-10-1.5N, Cellvis, USA). The coverslip was pre-coated with
446 50 μl of 50 μg/ml lectin (Sigma, L2380) and allowed to dry overnight at 4°C. The cells were
447 allowed to attach to the coverslip for 10 mins at room temperature before addition of another 2
448 ml EMM in the Petri dish.

449 We employed a spinning disk confocal microscope for fluorescence microscopy using an
450 Olympus IX71 unit equipped with a CSU-X1 spinning-disk unit (Yokogawa, Japan). The
451 motorized stage (ASI, USA) includes a Piezo Z Top plate for acquiring Z-series. The images
452 were captured on an EMCCD camera (IXON-897, Andor) controlled by iQ3.0 (Andor). Solid-
453 state lasers of 488 and 561 nm were used at a power of no more than 2.5 mW. Unless specified,
454 we used a 60×objective lens (Olympus, Plan Apochromat, NA = 1.40). A Z-series of 8 slices at a
455 spatial distance of 1 μm was captured at each time point. The microscopy was carried out in a
456 designated room maintained at 22 ± 2°C. To minimize environmental variations, we typically
457 imaged both control and experimental groups in randomized order on the same day.

458 We employed a CellASIC ONIX2 system controlled by a desktop computer through the
459 ONIX software (EMD Millipore) to apply osmotic shock. Using yeast haploid microfluidics
460 plate (Y04C, EMD Millipore), we pushed the cells into the imaging chamber at a pressure of 5-8
461 PSI for a minimum of 2 minutes using EMM media. The trapped cells were equilibrated in EMM
462 for 10 mins at a pressure of 1.45 PSI. The same pressure was applied for the media exchange
463 afterwards.

464 **Calcium imaging of fission yeast cells and data analysis**

465 To measure the intracellular calcium level of single fission yeast cells, we quantified the
466 fluorescence intensity of cells expressing GCaMP-mCherry (Poddar et al., 2021). Whenever a
467 temperature shift was required, cells were imaged after incubation at 36ºC for 4 hours. The
468 fluorescence intensity of each cell was quantified using average intensity projections of the Z-
469 series after the background subtraction. To measure the intracellular fluorescence, we quantified
470 the average fluorescence intensity on a line drawn along the long axis of a cell. Background
471 fluorescence was calculated similarly by measuring the areas without any cells.

472 For time-lapse measurement of calcium spikes, we quantified the fluorescence intensity
473 of cells expressing GCaMP. The GCaMP fluorescence was quantified from the average intensity
474 projection of the Z-series on a line along the long axis of a cell throughout osmotic shock. The
475 fluorescence intensities were background subtracted and normalized to the average value before
476 application of osmotic shock. Amplitudes of a calcium spike were defined as $\Delta F/F_0$. ΔF equals to
477 F_{max}, the maximum value during the first ten minutes after osmotic shock, minus the baseline
478 value F_0, calculated as the average of the five data points before osmotic shock.

479 **Computation-assisted quantification of cytokinetic calcium spikes**

480 We applied custom-written software to extract the parameters of cytokinetic calcium spikes from
481 time-lapse microscopy. Specifically, the analysis of the separation spikes was performed in two
482 separate segments, prior and post to cell separation. The first step of this analysis involves
483 removal of background noise to increase the signal to noise ratio (SNR) by preprocessing the
484 image sequences extracted from the videos. The images were passed through a median filter,
485 which smoothens the images while preserving their spatiotemporal resolution. The background
486 fluorescence was removed by subtracting the temporal average of each median-filtered pixel
487 value from the median-filtered images at each time point. A binary mask was generated by

488 further subtracting the average pixel value of each frame and binarizing the images using Otsu's
489 thresholding method. The signal from individual cells were identified by applying the binary
490 mask on the median-filtered background-subtracted images and the average fluorescence
491 intensity value per pixel was calculated for each frame. For post-cell separation, the two daughter
492 cells were analyzed separately. The aforementioned steps were also applied on the daughter cells
493 separately, i.e. median filtering followed by background subtraction and application of the binary
494 mask. Additionally, we applied a size-based filter to digitally eliminate any other fragments of
495 cells that may be present within the field of view and interfere with the analysis. This filtering
496 was done by detecting the objects (cells) and calculating their area. Any object with size below a
497 pre-set cutoff was eliminated from Analysis. The cut-off size was manually calculated based on
498 the average of more than 20 different cells.

499 The time dependent average fluorescence intensity (per pixel in each frame) was recorded
500 for each cell both before and after the cell separation. Temporal averaging of the signal was
501 performed in order to eliminate any minute fluctuations within the data and intensity values
502 lower than a threshold value was nullified. The locations of the peaks are defined by the point of
503 inversion of the derivative from positive to negative. These locations (frame number/timepoint)
504 and the average fluorescence intensity values corresponding to these time points were recorded
505 and used for analysis.

506 The temporal average of the baseline fluorescence intensity value (per pixel) was
507 calculated by applying the binary mask on the original images without any preprocessing. The
508 baseline for the parent cell and the two daughter cells were calculated separately. The video
509 processing and analysis was performed by implementing our custom developed code in
510 MATLAB (MathWorks, MA).

Acknowledgments

This work has been supported by National Institutes of Health grants R21GM134167 and R01 EB030031 to AL. It has also been supported by the National Institutes of Health grants R15GM134496 and R01GM144652 to QC. FZ has been supported by the University of Toledo Undergraduate Summer Research and Creative Activities Program. The content is solely the responsibility of the authors and does not necessarily represent the official views of the National Institutes of Health. The authors declare no competing interests.

518 **Figure and Figure Legends**
519

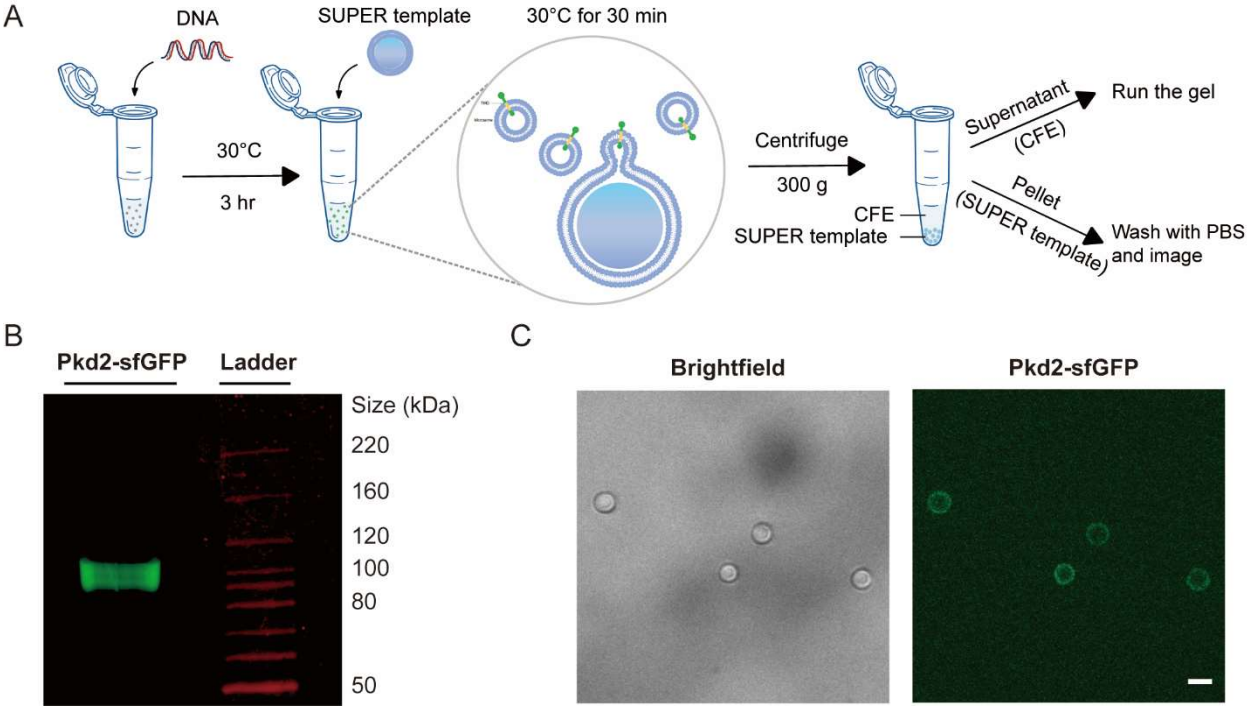

520

521 **Figure 1: Localization of cell-free expressed Pkd2 in SUPER template. (A)** Schematic
522 illustrating the use of CFE for in vitro protein production and testing the incorporation of
523 membrane proteins by using SUPER templates. SUPER templated beads are added to the CFE
524 reaction expressing Pkd2 protein fused to sfGFP at the C-terminus and incubated together. CFE
525 reaction and SUPER templates are then isolated by low-speed centrifugation for running a gel or
526 imaging, respectively. **(B)** Fluorescence gel image of cell-free expressed Pkd2-sfGFP added to
527 SUPER templates. **(C)** Brightfield and fluorescence micrograph of SUPER templates incubated
528 with cell-free expressed Pkd2-sfGFP. Beads were washed with PBS before imaging. Scale bar:
529 10 µm.

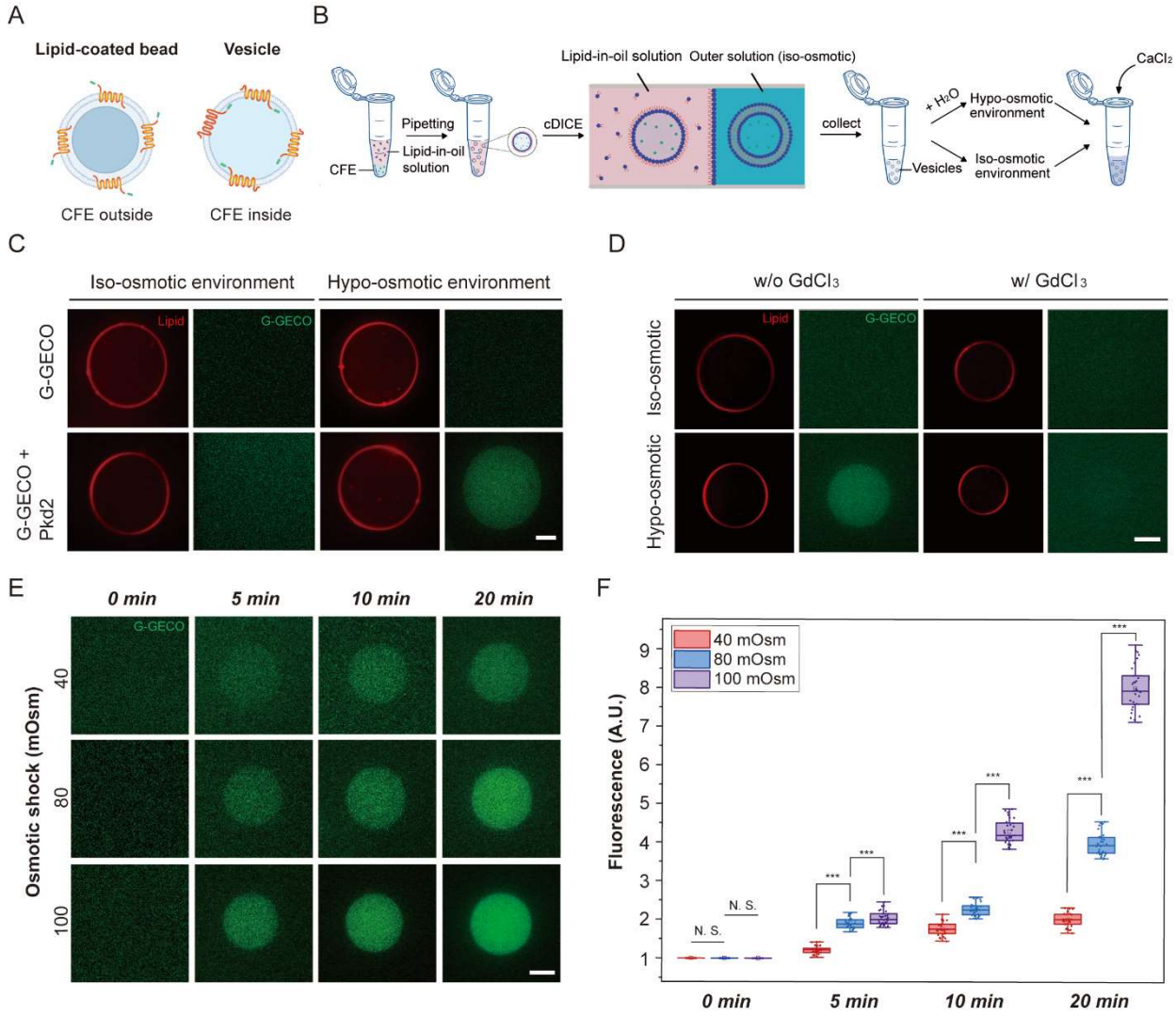

Figure 2: Pkd2 reconstituted in GUVs responds to osmotic pressure. **(A)** Schematic illustrating the directional insertion of cell-free expressed Pkd2 protein into the lipid bilayer membrane of SUPER templated beads and GUVs. Pkd2 channels are oriented with their C-termini protruding away from the lipid-coated beads and with their C-termini pointing inside the vesicles. **(B)** Schematic illustrates the formation of vesicles encapsulating cell-free expressed proteins using cDICE, followed by applying osmotic shock to Pkd2-containing GUVs. Vesicles were formed in iso-osmotic conditions and then milli-Q water was added to the outer solution to create a hypo-osmotic environment. 100 mM $CaCl_2$ stock solution is added to the hypo-osmotic external solution to a final concentration of 10 mM. **(C)** Representative fluorescence micrographs of vesicles encapsulating 1 mM EGTA and cell-free expressed Pkd2 and G-GECO at t =10 min after applying osmotic shock. Plasmid concentrations of Pkd2 and G-GECO were fixed at 1 nM. The final concentration of Ca^{2+} in the hypo-osmotic external solution was 10 mM. The aqueous external solution was made by diluting the external solution stock (HEPES: $MgCl_2$: KCl: glucose (in mM) = 15:3:150:50) with milli-Q water. The osmolarity difference between iso-osmotic and hypo-osmotic solutions was kept at 100 mOsm. **(D)** Representative fluorescence micrographs of vesicles expressing Pkd2 and G-GECO with addition of $GdCl_3$ for blocking the

547 force-activated function of Pkd2 channels under osmotic shock. $GdCl_3$ was added to the outer
548 solution with the final concentration fixed at 1 mM. The same method and solutions/conditions
549 described in (C) applied osmotic pressure to the vesicles. The images were taken 15 minutes
550 after the application of osmotic shock. Vesicles expressing Pkd2 and G-GECO without the
551 addition of $GdCl_3$ served as a control. **(E)** Representative fluorescence micrographs of vesicles
552 encapsulating cell-free expressed Pkd2 and G-GECO under different hypo-osmotic environments
553 at specified time points. The concentrations of EGTA, Pkd2, G-GECO, and Ca^{2+} were the same
554 as indicated in (C). **(F)** Box plot depicting the fluorescence intensities of vesicles under different
555 osmotic conditions and times. At least thirty vesicles were analyzed for each condition. All
556 experiments were repeated three times under identical conditions. Scale bars: 10 μm. ***: $P <$
557 0.001.
558

559

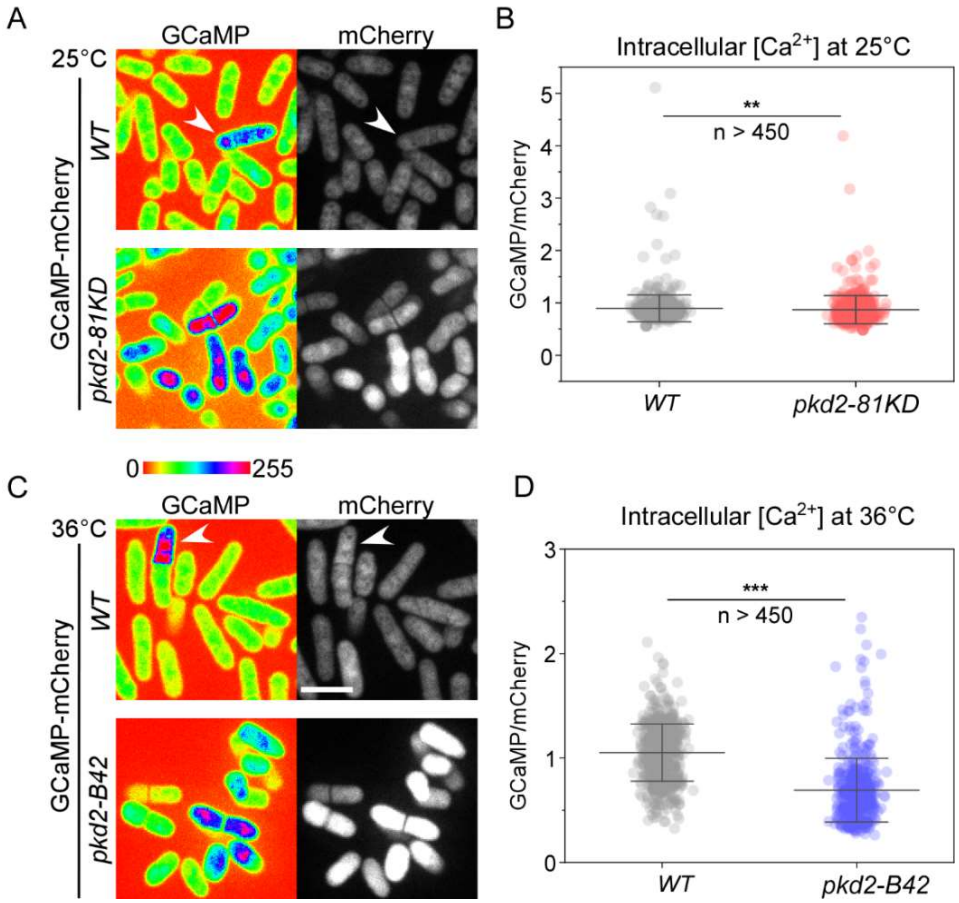

Figure 3: Intracellular calcium level was reduced in *pkd2* mutant cells. The intracellular calcium level of *wild type* (*WT*) and *pkd2* mutant cells at either the permissive temperature of 25°C (A and B) or the restrictive temperature of 36°C (C and D). **(A and C)** Representative fluorescence micrographs of *wild type* (top) and *pkd2* mutant (bottom) cells expressing GCaMP-mCherry. Arrowhead: a cell with elevated calcium level. **(B and D)** Scatter interval plot of intracellular calcium level of the *wild type* and the *pkd2* mutant cells. The average calcium level of *pkd2-81KD* cells was 3% lower than that of *wild type* cells. In contrast, the average calcium level of *pkd2-B42* cells was 34% lower than the *wild type* at 36°C. All data are pooled from three biological repeats. **: $P < 0.01$. ***: $P < 0.001$. Two-tailed student t-tests with unequal variants were used. Scale bars: 10 μm.

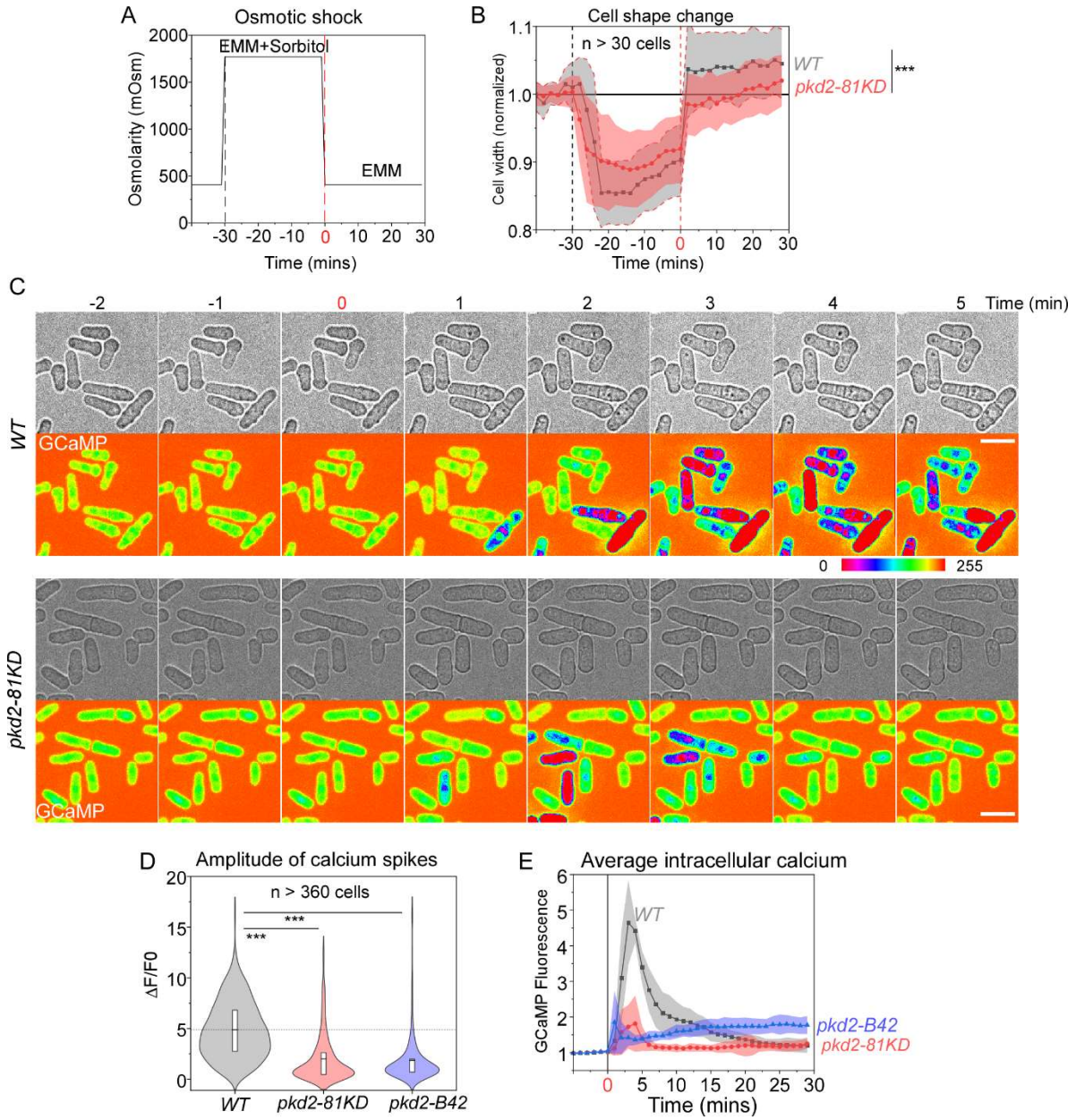

Figure 4: Pkd2 mutations reduced calcium spikes triggered by hypo-osmotic shock. (A) Time course of the osmolarity of the extracellular environment in the microfluidics chamber. Time zero: application of hypo-osmotic shock through replacing EMM plus 1.2M sorbitol with EMM media. **(B)** Time course of the cell width changes during the hypo-osmotic shock. Cloud represents standard deviations. Both *wild type* (*WT*) and *pkd2-81KD* cells expanded their cell width significantly after shock, but the *wild type* expanded more than the *pkd2-81KD* mutant. **(C)** Time-lapse micrographs of *wild type* and *pkd2-81KD* cells expressing GCaMP. The hypo-osmotic shock triggered calcium spikes. **(D)** Violin plot comparing calcium spikes amplitude of *wild type*, *pkd2-81KD,* and *pkd2-B42* cells (n > 360). **(E)** Time course of normalized GCaMP fluorescence during hypo-osmotic shock. Cloud represents standard deviations. All data are pooled from at least three biological repeats. ***: $P < 0.001$. Two-tailed student t-tests with unequal variants were used. Scale bars: 10 μm.

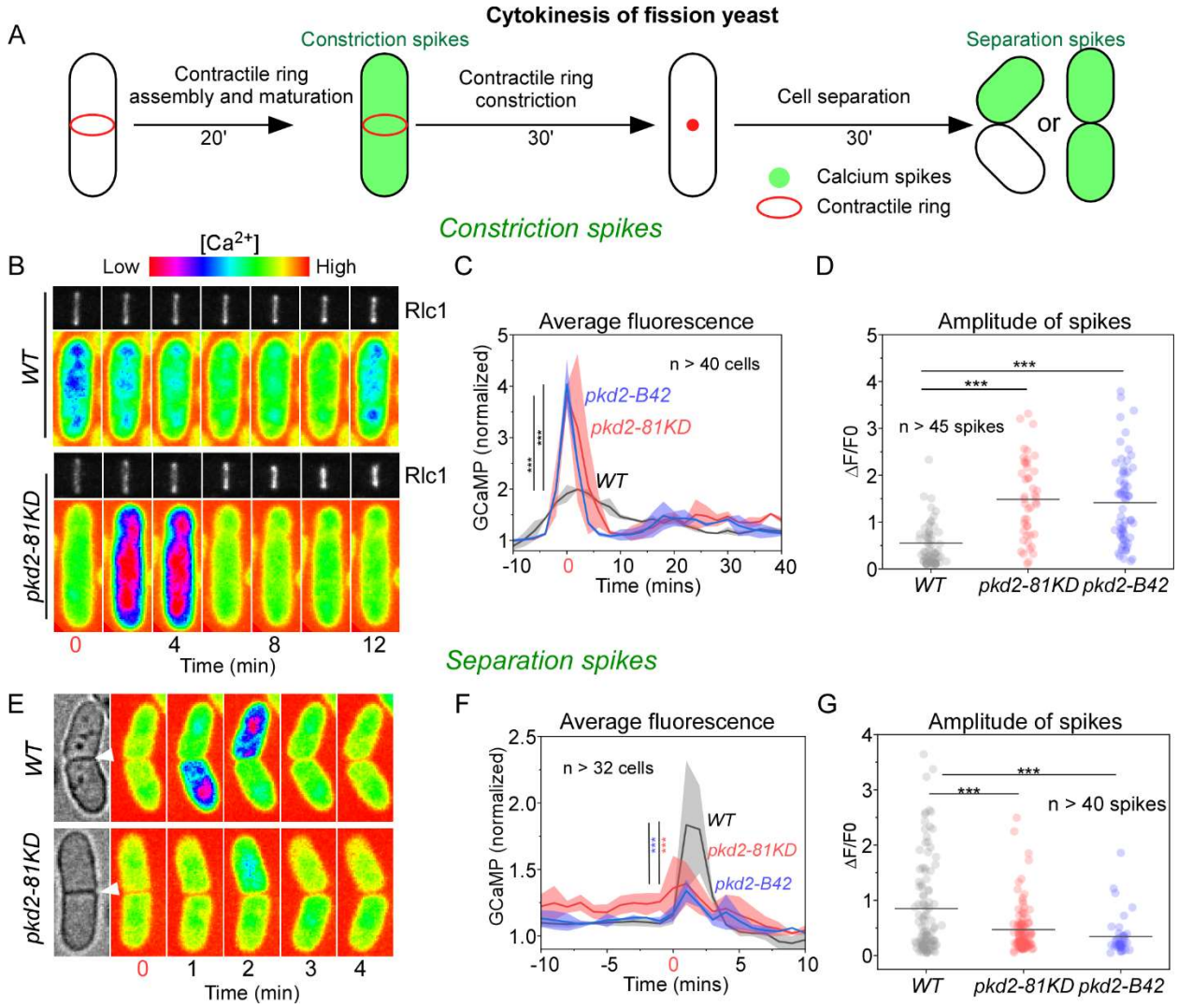

Figure 5: Pkd2 mutations reduced the separation calcium spikes.
(A) Diagram of the time course of cytokinetic calcium spikes in fission yeast cells. **(B-D)** Mutations of *pkd2* enhanced the constriction calcium spikes. **(B)** Time-lapse micrographs of a wild type (WT) and a *pkd2-81KD* cell expressing both GCaMP (pseudo-colored) and Rlc1-tdtomato (gray). Number: the time after the start of the contractile ring constriction. **(C)** Time courses of the average GCaMP fluorescence of the wild type and two *pkd2* mutants *(pkd2-81KD and pkd2-B42)* cells (n>40) throughout the contractile ring constriction. Cloud represents standard deviation. **(D)** Dot plot of the peak amplitude of the constriction spikes. Line: average. **(E-G)** Mutations of *pkd2* reduced the separation calcium spikes. **(E)** Time-lapse micrographs of separating wild type (WT) and *pkd2-81KD* cells expressing GCaMP (pseudo-colored). Number: the time after the cell separation. Arrowhead: cell separation. **(F)** Time course of the average GCaMP fluorescence of the wild type and two *pkd2* mutants *(pkd2-81KD and pkd2-B42)* cells (n>32). Cloud represents standard deviation. **(G)** Dot plot of the peak amplitude of the separation calcium spikes. Line: average. All the data are pooled from at least three independent biological repeats. ***: P < 0.001 (Two-tailed student t-test).

References

Balasubramanian, M.K., D. McCollum, L. Chang, K.C. Wong, N.I. Naqvi, X. He, S. Sazer, and K.L. Gould. 1998. Isolation and characterization of new fission yeast cytokinesis mutants. *Genetics*. 149:1265-1275.

Barr, M.M., and P.W. Sternberg. 1999. A polycystic kidney-disease gene homologue required for male mating behaviour in C. elegans. *Nature*. 401:386-389.

Bashirzadeh, Y., N. Wubshet, T. Litschel, P. Schwille, and A.P. Liu. 2021. Rapid Encapsulation of Reconstituted Cytoskeleton inside Giant Unilamellar Vesicles. *J Vis Exp*.

Batiza, A.F., T. Schulz, and P.H. Masson. 1996. Yeast respond to hypotonic shock with a calcium pulse. *The Journal of biological chemistry*. 271:23357-23362.

Chong, S. 2014. Overview of cell-free protein synthesis: historic landmarks, commercial systems, and expanding applications. *Curr Protoc Mol Biol*. 108:16 30 11-11.

Dondapati, S.K., M. Kreir, R.B. Quast, D.A. Wustenhagen, A. Bruggemann, N. Fertig, and S. Kubick. 2014. Membrane assembly of the functional KcsA potassium channel in a vesicle-based eukaryotic cell-free translation system. *Biosens Bioelectron*. 59:174-183.

Forman, J.R., S. Qamar, E. Paci, R.N. Sandford, and J. Clarke. 2005. The remarkable mechanical strength of polycystin-1 supports a direct role in mechanotransduction. *Journal of molecular biology*. 349:861-871.

Gao, Z., D.M. Ruden, and X. Lu. 2003. PKD2 cation channel is required for directional sperm movement and male fertility. *Curr Biol*. 13:2175-2178.

Gonzalez-Perrett, S., K. Kim, C. Ibarra, A.E. Damiano, E. Zotta, M. Batelli, P.C. Harris, I.L. Reisin, M.A. Arnaout, and H.F. Cantiello. 2001. Polycystin-2, the protein mutated in autosomal dominant polycystic kidney disease (ADPKD), is a Ca2+-permeable nonselective cation channel. *Proceedings of the National Academy of Sciences of the United States of America*. 98:1182-1187.

Gregorio, N.E., M.Z. Levine, and J.P. Oza. 2019. A User's Guide to Cell-Free Protein Synthesis. *Methods Protoc*. 2.

Hirayama, S., R. Sugiura, Y. Lu, T. Maeda, K. Kawagishi, M. Yokoyama, H. Tohda, Y. Giga-Hama, H. Shuntoh, and T. Kuno. 2003. Zinc finger protein Prz1 regulates Ca2+ but not Cl- homeostasis in fission yeast. Identification of distinct branches of calcineurin signaling pathway in fission yeast. *The Journal of biological chemistry*. 278:18078-18084.

Huang, K., D.R. Diener, A. Mitchell, G.J. Pazour, G.B. Witman, and J.L. Rosenbaum. 2007. Function and dynamics of PKD2 in Chlamydomonas reinhardtii flagella. *The Journal of cell biology*. 179:501-514.

Hughes, J., C.J. Ward, B. Peral, R. Aspinwall, K. Clark, J.L. San Millan, V. Gamble, and P.C. Harris. 1995. The polycystic kidney disease 1 (PKD1) gene encodes a novel protein with multiple cell recognition domains. *Nature genetics*. 10:151-160.

Jia, B., and C.O. Jeon. 2016. High-throughput recombinant protein expression in Escherichia coli: current status and future perspectives. *Open Biol*. 6.

Jumper, J., R. Evans, A. Pritzel, T. Green, M. Figurnov, O. Ronneberger, K. Tunyasuvunakool, R. Bates, A. Zidek, A. Potapenko, A. Bridgland, C. Meyer, S.A.A. Kohl, A.J. Ballard, A. Cowie, B. Romera-Paredes, S. Nikolov, R. Jain, J. Adler, T. Back, S. Petersen, D. Reiman, E. Clancy, M. Zielinski, M. Steinegger, M. Pacholska, T. Berghammer, S. Bodenstein, D. Silver, O. Vinyals, A.W. Senior, K. Kavukcuoglu, P. Kohli, and D. Hassabis. 2021. Highly accurate protein structure prediction with AlphaFold. *Nature*.

Khambhati, K., G. Bhattacharjee, N. Gohil, D. Braddick, V. Kulkarni, and V. Singh. 2019. Exploring the Potential of Cell-Free Protein Synthesis for Extending the Abilities of Biological Systems. *Front Bioeng Biotechnol*. 7:248.

Knol, J., K. Sjollema, and B. Poolman. 1998. Detergent-mediated reconstitution of membrane proteins. *Biochemistry*. 37:16410-16415.

646 Laohakunakorn, N., L. Grasemann, B. Lavickova, G. Michielin, A. Shahein, Z. Swank, and S.J. Maerkl. 2020.
647 Bottom-Up Construction of Complex Biomolecular Systems With Cell-Free Synthetic Biology.
648 *Front Bioeng Biotechnol*. 8:213.
649 Lima, W.C., A. Vinet, J. Pieters, and P. Cosson. 2014. Role of PKD2 in rheotaxis in Dictyostelium. *PLoS One*.
650 9:e88682.
651 Liu, X., T. Vien, J. Duan, S.H. Sheu, P.G. DeCaen, and D.E. Clapham. 2018. Polycystin-2 is an essential ion
652 channel subunit in the primary cilium of the renal collecting duct epithelium. *eLife*. 7.
653 Lu, Y. 2017. Cell-free synthetic biology: Engineering in an open world. *Synth Syst Biotechnol*. 2:23-27.
654 Majumder, S., J. Garamella, Y.L. Wang, M. DeNies, V. Noireaux, and A.P. Liu. 2017. Cell-sized
655 mechanosensitive and biosensing compartment programmed with DNA. *Chem Commun (Camb)*.
656 53:7349-7352.
657 Majumder, S., P.T. Willey, M.S. DeNies, A.P. Liu, and G.W.G. Luxton. 2018. A synthetic biology platform
658 for the reconstitution and mechanistic dissection of LINC complex assembly. *J Cell Sci*. 132.
659 Majumder, S., P.T. Willey, M.S. DeNies, A.P. Liu, and G.W.G. Luxton. 2019. Correction: A synthetic biology
660 platform for the reconstitution and mechanistic dissection of LINC complex assembly
661 (doi:10.1242/jcs.219451). *J Cell Sci*. 132.
662 Maundrell, K. 1990. nmt1 of fission yeast. A highly transcribed gene completely repressed by thiamine.
663 *The Journal of biological chemistry*. 265:10857-10864.
664 Mochizuki, T., G. Wu, T. Hayashi, S.L. Xenophontos, B. Veldhuisen, J.J. Saris, D.M. Reynolds, Y. Cai, P.A.
665 Gabow, A. Pierides, W.J. Kimberling, M.H. Breuning, C.C. Deltas, D.J. Peters, and S. Somlo. 1996.
666 PKD2, a gene for polycystic kidney disease that encodes an integral membrane protein. *Science*
667 *(New York, N.Y)*. 272:1339-1342.
668 Moreno, S., A. Klar, and P. Nurse. 1991. Molecular genetic analysis of fission yeast Schizosaccharomyces
669 pombe. *Methods in enzymology*. 194:795-823.
670 Morris, Z., D. Sinha, A. Poddar, B. Morris, and Q. Chen. 2019. Fission yeast TRP channel Pkd2p localizes to
671 the cleavage furrow and regulates cell separation during cytokinesis. *Molecular biology of the cell*.
672 30:1791-1804.
673 Nakayama, Y., K. Yoshimura, and H. Iida. 2012. Organellar mechanosensitive channels in fission yeast
674 regulate the hypo-osmotic shock response. *Nature communications*. 3:1020.
675 Nauli, S.M., F.J. Alenghat, Y. Luo, E. Williams, P. Vassilev, X. Li, A.E. Elia, W. Lu, E.M. Brown, S.J. Quinn, D.E.
676 Ingber, and J. Zhou. 2003. Polycystins 1 and 2 mediate mechanosensation in the primary cilium of
677 kidney cells. *Nature genetics*. 33:129-137.
678 Neumann, S., T.J. Pucadyil, and S.L. Schmid. 2013. Analyzing membrane remodeling and fission using
679 supported bilayers with excess membrane reservoir. *Nat Protoc*. 8:213-222.
680 Palmer, C.P., E. Aydar, and M.B. Djamgoz. 2005. A microbial TRP-like polycystic-kidney-disease-related ion
681 channel gene. *The Biochemical journal*. 387:211-219.
682 Pittman, J.K. 2011. Vacuolar Ca(2+) uptake. *Cell calcium*. 50:139-146.
683 Poddar, A., O. Sidibe, A. Ray, and Q. Chen. 2021. Calcium spikes accompany cleavage furrow ingression
684 and cell separation during fission yeast cytokinesis. *Molecular biology of the cell*. 32:15-27.
685 Protchenko, O., R. Rodriguez-Suarez, R. Androphy, H. Bussey, and C.C. Philpott. 2006. A screen for genes
686 of heme uptake identifies the FLC family required for import of FAD into the endoplasmic
687 reticulum. *The Journal of biological chemistry*. 281:21445-21457.
688 Pucadyil, T.J., and S.L. Schmid. 2008. Real-time visualization of dynamin-catalyzed membrane fission and
689 vesicle release. *Cell*. 135:1263-1275.
690 Pucadyil, T.J., and S.L. Schmid. 2010. Supported bilayers with excess membrane reservoir: a template for
691 reconstituting membrane budding and fission. *Biophys J*. 99:517-525.
692 Rigaud, J.L., and D. Levy. 2003. Reconstitution of membrane proteins into liposomes. *Methods Enzymol*.
693 372:65-86.

694 Shen, P.S., X. Yang, P.G. DeCaen, X. Liu, D. Bulkley, D.E. Clapham, and E. Cao. 2016. The Structure of the
695 Polycystic Kidney Disease Channel PKD2 in Lipid Nanodiscs. *Cell*. 167:763-773 e711.
696 Sinha, D., D. Ivan, E. Gibbs, M. Chetluru, J. Goss, and Q. Chen. 2022. Fission yeast polycystin Pkd2p
697 promotes cell size expansion and antagonizes the Hippo-related SIN pathway. *Journal of cell*
698 *science*. 135.
699 Van de Cauter, L., F. Fanalista, L. van Buren, N. De Franceschi, E. Godino, S. Bouw, C. Danelon, C. Dekker,
700 G.H. Koenderink, and K.A. Ganzinger. 2021. Optimized cDICE for Efficient Reconstitution of
701 Biological Systems in Giant Unilamellar Vesicles. *ACS Synth Biol*. 10:1690-1702.
702 Verde, F., D.J. Wiley, and P. Nurse. 1998. Fission yeast orb6, a ser/thr protein kinase related to mammalian
703 rho kinase and myotonic dystrophy kinase, is required for maintenance of cell polarity and
704 coordinates cell morphogenesis with the cell cycle. *Proceedings of the National Academy of*
705 *Sciences of the United States of America*. 95:7526-7531.
706 Vjestica, A., M. Marek, P.J. Nkosi, L. Merlini, G. Liu, M. Berard, I. Billault-Chaumartin, and S.G. Martin. 2020.
707 A toolbox of stable integration vectors in the fission yeast Schizosaccharomyces pombe. *J Cell Sci*.
708 133.
709 Wang, Z., C. Ng, X. Liu, Y. Wang, B. Li, P. Kashyap, H.A. Chaudhry, A. Castro, E.M. Kalontar, L. Ilyayev, R.
710 Walker, R.T. Alexander, F. Qian, X.Z. Chen, and Y. Yu. 2019. The ion channel function of polycystin-
711 1 in the polycystin-1/polycystin-2 complex. *EMBO reports*. 20:e48336.
712 Wingfield, P.T. 2015. Overview of the purification of recombinant proteins. *Curr Protoc Protein Sci*. 80:6 1
713 1-6 1 35.
714 Xu, S., W.A. Cramer, A.A. Peterson, M. Hermodson, and C. Montecucco. 1988. Dynamic properties of
715 membrane proteins: reversible insertion into membrane vesicles of a colicin E1 channel-forming
716 peptide. *Proc Natl Acad Sci U S A*. 85:7531-7535.
717 Zhou, X.L., and C. Kung. 1992. A mechanosensitive ion channel in Schizosaccharomyces pombe. *The EMBO*
718 *journal*. 11:2869-2875.

719